Acoustic Wave Focusing From Reconfigurable Acoustic Arrays Based on a Bricard-Miura Synthesis

Christopher S. Bentley
Department of Mechanical Engineering,
The Pennsylvania State University,
University Park, PA 16802
e-mail: csb5532@psu.edu

Ryan L. Harne[1]
Department of Mechanical Engineering,
The Pennsylvania State University,
University Park, PA 16802
e-mail: ryanharne@psu.edu

Recent studies have shown that reconfigurable acoustic arrays inspired from rigid origami structures can be used to radiate and focus acoustic waves. Yet, there is a need for exploration of single-degree-of-freedom deployment to be integrated with such arrays for sake of tailoring wave focusing. This research explores a reconfigurable acoustic array inspired from a regular Miura-ori unit cell and threefold-symmetric Bricard linkage. The system focuses on acoustic waves and has single-degree-of-freedom motion when incorporated with a modified threefold-symmetric Bricard linkage. Three configurations of the array are analyzed where array facets that converge towards the center axis are considered to vibrate like baffled pistons and generate acoustic waves into the surrounding fluid. An analytical model is constructed to explore the near-field acoustic focusing behavior of the proposed acoustic array. The wave focusing capabilities of the array are verified through proof-of-principle experiments. The results show that the wave focusing of the array is influenced by the geometric parameters of the facets and the relative distance of facets to the center axis, in agreement with simplified ray acoustics estimates. These findings underscore the fundamental relationship between focusing sound radiators and geometric acoustics principles. The results encourage broader exploration of acoustic array designs inspired from integrated single-degree-of-freedom linkages and origami structures for sake of straightforward array deployment and reconfiguration. [DOI: 10.1115/1.4054252]

Keywords: origami mechanisms, acoustic arrays, reconfigurable structures, structural acoustics

1 Introduction

The application of origami-inspired structures in science and engineering fields is extensive because it provides new ways of approaching the design of complex three-dimensional (3D) structures that are portable, reconfigurable, and lightweight. Researchers in fields such as space exploration, medicine, and robotics have studied origami-based folding for solar arrays [1–3], satellite antennas [4–6], biomedical devices [7–9], and soft robots [10–12]. Deployable shelters also exploit the portability and reconfigurability of origami folding [13].

Additionally, origami-based structures have been introduced to the field of acoustic wave focusing. Traditional wave focusing techniques adjust the wave phase and amplitude of the transducer elements with digital controls to emulate the physical realignment of transducers for wave convergence [14,15]. An important application of acoustic wave focusing in medicine is the use of high-intensity focused ultrasound (HIFU) to ablate cancerous tumors within the body [16]. Yet, certain cancerous tumors in the body can be inaccessible for HIFU treatment, due to the size of the transducer array in comparison to the tumor location [16]. Recent studies have shown that acoustic transducer arrays inspired from rigid origami such as Miura-ori can focus acoustic waves and be reconfigured to reduce the array size during transport stages [17,18].

To advance these research efforts, Zhao et al. [19] have explored the integration of waterbomb origami or deployable mechanisms such as the Hoberman ring [20] with regular Miura-ori facets to provide curvature for acoustic wave focusing and structural stability for deployment. Furthermore, Lang et al. [21] have proposed the usage of designed-offset linkages with rigid origami to achieve single-degree-of-freedom motion between the unfolded and folded states. Vlachaki and Liapi [22] have also proposed the usage of linkages with rigid origami by coupling scissor linkages to various origami crease patterns to provide single-degree-of-freedom motion and increased structural stability. While these researchers have demonstrated means to achieve low dimensional motion in origami structures via rigid body linkages, only the Hoberman ring [20] has been studied for reconfigurable arrays in acoustic wave focusing applications.

Alternatively, researchers have explored rigid link behavior that is embedded in zero-thickness rigid origami. For instance, Chen et al. [23] and Feng et al. [24] demonstrate that zero-thickness rigid origami patterns are comparable to rigid bar spherical linkages. In particular, rigid origami with a four-crease vertex has the same kinematic behavior as that of spherical linkages with four rotating joints. Moreover, several researchers have shown that the single-degree-of-freedom behavior of zero-thickness rigid origami can be retained for rigid origami with thick panels by replacing the spherical linkage behavior of the vertices with those of single-degree-of-freedom spatial linkages [25–28]. Yet, these research efforts only address the deployment behavior of origami-inspired structures without considering other physical phenomena, such as wave focusing, in the origami pattern design.

Motived by the shortcomings of these two approaches for exploring rigid origami deployment, the objective of this research is to construct and study an acoustic wave focusing array inspired from Miura-ori origami and the kinematic behavior of a modified threefold-symmetric Bricard linkage [29,30]. The array focuses acoustic waves according to the folded configuration resulting in convergent, sound-radiating facets. The crease pattern and

[1]Corresponding author.

Contributed by the Technical Committee on Vibration and Sound of ASME for publication in the Journal of Vibration and Acoustics. Manuscript received October 26, 2021; final manuscript received March 30, 2022; published online May 2, 2022. Assoc. Editor: Fabio Semperlotti.

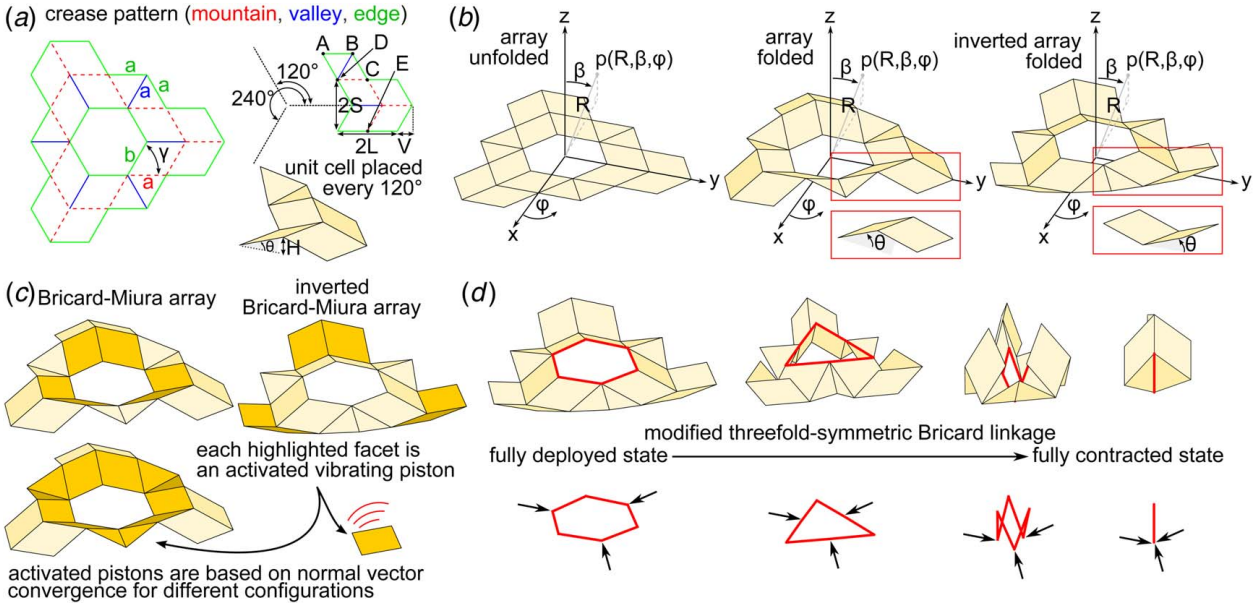

Fig. 1 (*a*) Folding patterns and geometric parameters for the Bricard-Miura array, (*b*) folded and unfolded configurations of the array with the acoustic field point defined in terms of spherical coordinates, (c) three candidate configurations for converging activated facets, and (*d*) single-degree-of-freedom motion of the Bricard-Miura array when a linkage inspired from the threefold-symmetric Bricard linkage is embedded on the inner edges of the array

geometric design parameters are shown in Fig. 1(*a*). The proposed array in unfolded, folded, and inverted folded configurations are shown in Fig. 1(*b*). As shown in Fig. 1(*c*), the regular Miura-ori facets are treated as vibrating baffled pistons. The selection of which facets to activate is intuitively based on the normal convergence of the facet planes to the central axis, as well as how close these normal vectors converge. Figure 1(*d*) shows that the rotational symmetry of the Miura-ori unit cells in the proposed acoustic array is inspired from and can incorporate a linkage inspired from the threefold-symmetric Bricard linkage [30] for single-degree-of-freedom motion.

Analytical and experimental efforts are utilized in this research to study the effects of facet normal vector convergence on wave focusing for the proposed acoustic array. Section 2 presents the analytical model used to scrutinize the wave focusing capabilities of the proposed acoustic array. Section 3 communicates the experimental efforts used to validate observations from the analytical model. Section 4 details the influences of the array facet normal vectors on acoustic convergence and wave focusing using theoretical investigations. Section 5 concludes the report by summarizing the new findings with closing remarks.

2 Analytical Model Formulation

In this section, the geometric model of a reconfigurable acoustic array is developed. A modified threefold-symmetric Bricard linkage is used to guide the reconfiguration of three regular Miura-ori unit cells. Direct acoustic radiation from the activated, vibrating Miura-ori facets is then analytically computed using Rayleigh's integral.

2.1 Kinematic Modeling of Bricard-Miura Array. Figure 1(*a*) shows the geometry of a regular Miura-ori unit cell combined with two triangular facets, which make up the Bricard-Miura unit cell. The regular Miura-ori unit cell has four facets governed by edge lengths a and b, facet angle γ, and folding angle θ. The regular, folded Miura-ori unit cell has dimensions H, S, L, and V, with relationships to the facet design parameters given by Schenk and Guest [31], as summarized in Eqs. (1)–(4)

$$H = a\sin\theta\sin\gamma = \sqrt{a^2 - L^2} \tag{1}$$

$$S = b\frac{\cos\theta\tan\gamma}{\sqrt{1+(\cos\theta\tan\gamma)^2}} \tag{2}$$

$$L = a\sqrt{1-(\sin\theta\sin\gamma)^2} \tag{3}$$

$$V = b\frac{1}{\sqrt{1+(\cos\theta\tan\gamma)^2}} \tag{4}$$

The edges for the two triangular facets have lengths equal to a and are connected together by vertices A, B, C, and D, as shown in Fig. 1(*a*). The vertices, C and D, are connected and defined by the corresponding Miura-ori unit cell vertices, as seen in Fig. 1(*a*). The 3D coordinates for vertex A are defined in Eq. (5)

$$\begin{pmatrix} A_x \\ A_y \\ A_z \end{pmatrix} = \begin{pmatrix} \cos\frac{2\pi}{3} & -\sin\frac{2\pi}{3} & 0 \\ \sin\frac{2\pi}{3} & \cos\frac{2\pi}{3} & 0 \\ 0 & 0 & 1 \end{pmatrix} \begin{pmatrix} E_x \\ E_y \\ E_z \end{pmatrix} \tag{5}$$

where E_x, E_y, and E_z are the coordinates for vertex E. The coordinates for vertex B are determined by solving for Eqs. (6)–(8)

$$a = \sqrt{(A_x - B_x)^2 + (A_y - B_y)^2 + (A_z - B_z)^2} \tag{6}$$

$$a = \sqrt{(D_x - B_x)^2 + (D_y - B_y)^2 + (D_z - B_z)^2} \tag{7}$$

$$a = \sqrt{(C_x - B_x)^2 + (C_y - B_y)^2 + (C_z - B_z)^2} \tag{8}$$

The coordinates for the remaining vertices on the Bricard-Miura array are then defined by Eq. (9)

$$\begin{pmatrix} n_x' \\ n_y' \\ n_z' \end{pmatrix} = \begin{pmatrix} \cos\alpha & -\sin\alpha & 0 \\ \sin\alpha & \cos\alpha & 0 \\ 0 & 0 & 1 \end{pmatrix} \begin{pmatrix} n_x \\ n_y \\ n_z \end{pmatrix} \tag{9}$$

where n_x, n_y, and n_z are the 3D coordinates for a given vertex on the Bricard-Miura unit cell, and α is the rotation angle set equal to $2\pi/3$ and $4\pi/3$ radians for the respective unit cell rotations.

2.2 Acoustic Modeling and Analysis. For the proposed acoustic array, the activated Miura-ori facets are assumed to be vibrating baffled pistons that radiate acoustic pressure in one direction only, based on support from previous research [18,32] and based on the specific experimental platform used here with baffled facet transducers, as shown in Sec. 3. Because of this assumption, Rayleigh's integral can be used to predict the directly radiated acoustic waves from the activated Miura-ori facets. Due to the effects of reflection and diffraction on the radiated sound field, it has been shown that Rayleigh's integral can only accurately predict the radiated acoustic pressure for small folding angles of the array [33]. As it is shown in Fig. 1(*b*), the acoustic pressure p is defined in spherical coordinates, where R is the radial distance, β is the elevation angle, φ is the azimuth angle, and the origin for the acoustic field is located at the geometric center of the unfolded acoustic array. The total acoustic pressure at a field point is computed by a linear superposition of all the activated facet contributions of acoustic pressure to the field point, where each facet contribution is determined from Rayleigh's integral. Equation (10) is the total acoustic pressure at the field point

$$p(R, \beta, \varphi, t) = j\frac{\rho_0 \omega u_0}{2\pi} e^{j\omega t} \sum_{n=1}^{N_f} \left[\int_{A_n} \frac{e^{-jkR_n}}{R_n} dA_n \right] \tag{10}$$

where ρ_0 is the atmospheric density of the fluid medium, ω is the angular frequency, u_0 is the amplitude of the normal particle velocity of the vibrating facet, N_f is the number of facets, A_n is the area of the nth facet, $k = \omega/c_0$ is the wavenumber where c_0 is the sound speed, and R_n is the distance from the center of the nth facet to the field point. Air is the fluid medium used in this study, where $\rho_0 = 1.21$ kg/m^3 and $c_0 = 343$ m/s.

Yet, Eq. (10) can only be evaluated analytically for a few special cases of geometry and field point locations. To determine the acoustic pressure in the near field for more arbitrary sound-radiating geometries like the reconfigurable acoustic array, Ocheltree and Frizzell [34] have developed a technique that discretizes the vibrating surfaces into infinitesimally small discrete point sources, where the distance between the point sources is much less than the acoustic wavelength and facet characteristic dimension. This technique is able to analytically evaluate the near-field acoustic pressure for arbitrary sound-radiating geometries because it represents a discretized and convergent approximation of the continuous Rayleigh's integral. The discretized version of Rayleigh's integral for this technique is given in Eq. (11)

$$p(R, \beta, \varphi, t) = j\frac{\rho_0 \omega u_0}{2\pi} e^{j\omega t} \sum_{n=1}^{N_f} \sum_{m=1}^{M} \left[\frac{e^{-jkR_{mn}}}{R_{mn}} A_{mn} \right] \tag{11}$$

where M is the number of discretized surfaces on a given facet, A_{mn} is the mth discretized surface element on the nth facet, and R_{mn} is the distance from the center of the mth discretized surface element on the nth facet to the field point. After the acoustic pressure is determined, the sound pressure level (SPL) is calculated using Eq. (12)

$$\text{SPL} = 20\log_{10}\left[\frac{p_{rms}(R, \beta, \varphi)}{p_{ref}}\right] \tag{12}$$

The $p_{rms}(R, \beta, \varphi)$ is the root-mean-square value of $p(R, \beta, \varphi)$, and $p_{ref} = 20\ \mu$Pa is the reference acoustic pressure for air.

3 Experimental Validation

Proof-of-concept specimens are fabricated so that acoustic wave focusing from the analytical models for the proposed array configurations can be experimentally validated. Wave focusing results from both experimental and analytical efforts are gathered and compared in this section.

3.1 Specimen Design and Fabrication. Experimental models are constructed for both the folded and inverted folded configurations of the proposed acoustic array. The arrays are fabricated with 1.59-mm-thick polypropylene sheets that are laser cut with the crease pattern from Fig. 1(*a*) and are shown in Figs. 2(*a*) and 2(*b*), respectively. The dimensions for the three Miura-ori facets on each configuration are $\gamma = 60$ deg and $a = b =$ 40.64 mm. For the inverted folded configuration of the array, the non-activated inner facets are removed to minimize the effects of diffraction on the measured sound pressure (Fig. 2(*b*)). Activated facets are emulated in the proof-of-concept specimens by circular miniature loudspeakers (Parts Express, Springboro, OH) bonded to centered

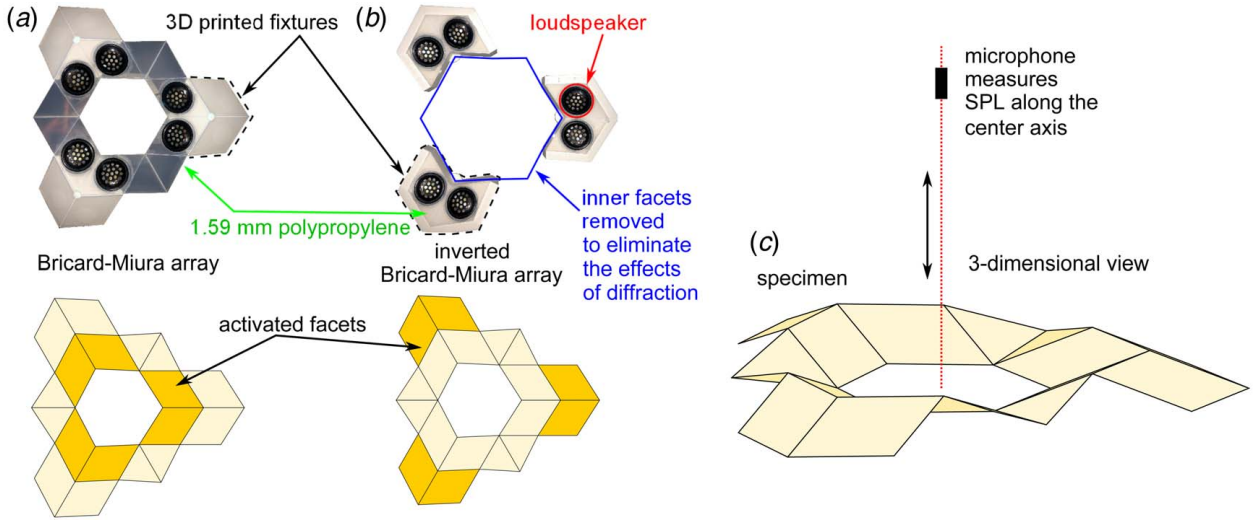

Fig. 2 (*a*) Proof-of-concept specimen and corresponding analytical model schematic for the Bricard-Miura array, (*b*) proof-of-concept specimen and corresponding analytical model schematic for the inverted Bricard-Miura array, and (*c*) three-dimensional schematic of the experiment setup, where the microphone measures the axial sound pressure level

laser-cut holes of passive panels at the activated facet positions. Each loudspeaker covers approximately 50% of the corresponding facet area. Support fixtures with fixed angles are constructed with a 3D printer (FlashForge Creator Pro) using acrylonitrile butadiene styrene (ABS) and fastened to each array configuration to position the proof-of-concept specimens at the prescribed folding angles. The miniature loudspeakers are driven at the same frequency with an external amplifier and function generator.

3.2 Experimental Setup. A hemi-anechoic acoustic chamber with dimensions 4 m × 4.25 m × 2.75 m is used to measure the near-field acoustic pressure generated by the proof-of-concept specimens. A microphone (PCB Piezotronics 130F20, Depew, NY) is used to measure the acoustic pressure along the central axis of the specimen, starting at the plane of the unfolded array, as shown in Fig. 2(*c*). A function generator is used to generate a tonal signal that is sent to an amplifier that drives the loudspeakers of the array. Measured acoustic pressure data are post-processed using MATLAB to determine the sound pressure level along the axial direction.

3.3 Comparison Between Experimental and Analytical Results. A comparison between the sound pressure level results from the experimental and analytical models is presented in Fig. 3. The normal surface velocity amplitude is determined to be 0.05 mm/s for the driving frequencies. In Fig. 3, the results are displayed with the horizontal axes representing the locations of the sound pressure levels along the center axis, starting at the plane of the unfolded array. The vertical axes represent the corresponding sound pressure levels for those locations. For each Bricard-Miura array configuration in Fig. 3, there is a peak SPL at an axial location close to the plane of the unfolded array. This axial location represents the acoustic near field where the acoustic pressure from the activated facets constructively converge and produce acoustic pressure focusing as is seen in the SPL peaks. The results in Fig. 3 also show local maxima in both the analytical and experimental models. The local maxima observed around 0.04 m in the analytical models (see Figs. 3(*a*)–3(*c*)) are due to constructive interference of the acoustic waves, whereas the local maxima in the experimental results are caused by a combination of the effects from diffraction, reflection, and the directly radiated waves.

In Fig. 3(*a*), the results for the analytical model of the Bricard-Miura array are presented for three folding angles of 15 deg, 20 deg, and 25 deg. A driving frequency of 19 kHz has been selected for experimental validation of the Bricard-Miura array due to its notable wave focusing capabilities for various folding angles of the array, as seen in Fig. 3. For a folding angle of 25 deg, the peak SPL is around 67 dB at an axial distance of 0.1 m (5.54 wavelengths). As the folding angle reduces to 20 deg and 15 deg, the peak SPL also reduces to around 66 dB and 65 dB with an increasing axial distance around 0.12 m and 0.13 m, respectively. Figure 3(*b*) displays the corresponding experimental results. For a folding angle of 25 deg and a driving frequency of 19 kHz, the peak SPL reaches 67 dB around an axial distance of 0.06 m. The experimental results also suggest that for folding angles of 20 deg and 15 deg, the peak SPL reaches 63 dB at 0.11 m and 61 dB at 0.12 m, respectively. When compared to Fig. 3(*a*), there is qualitative agreement with the acoustic focusing trends for increasing folding angles at axial distances less than 0.2 m despite the discrepancies for exact SPL and axial distance values. These discrepancies are due to the diffraction and reflection of acoustic waves from adjoining facets, as well as the assumption

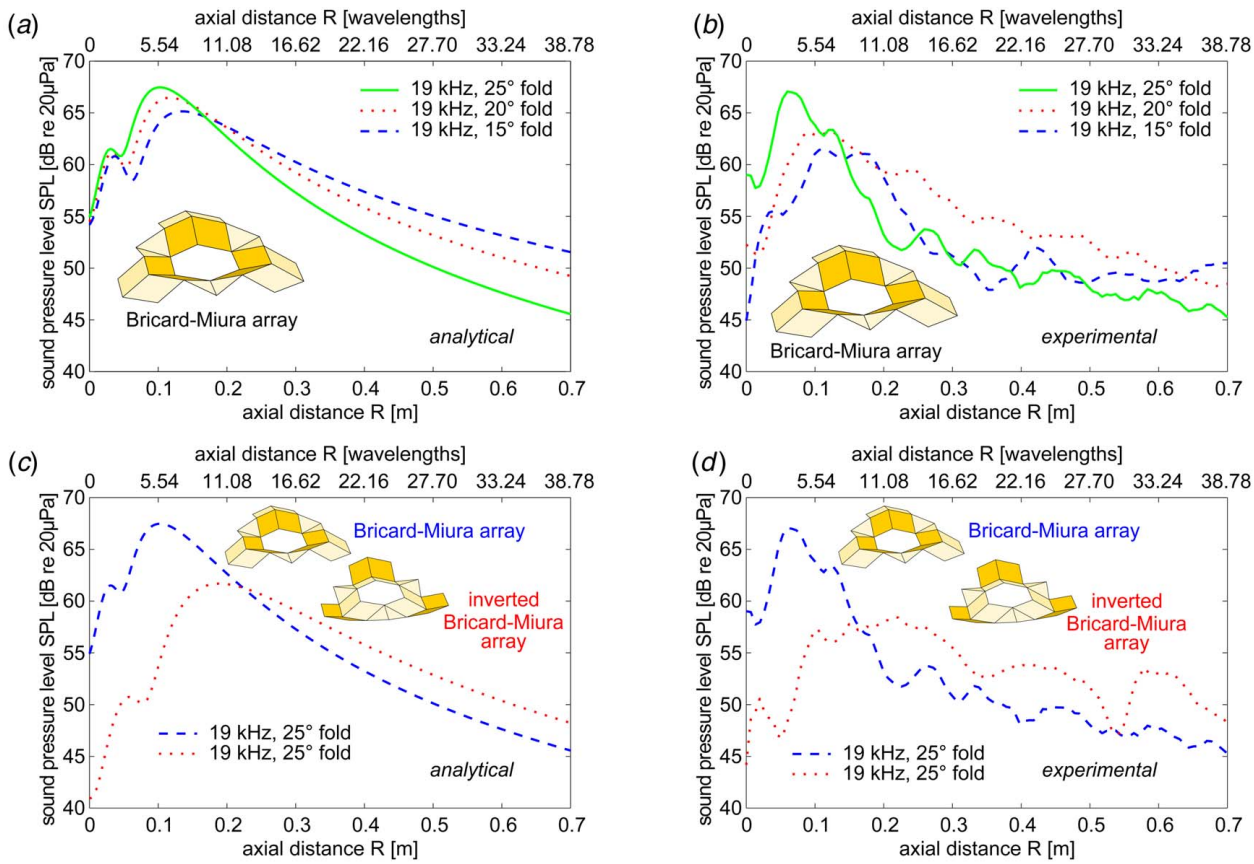

Fig. 3 Comparison of experimental and analytical results of sound pressure level as a function of axial distance: (*a*) the analytical results for the influence of facet folding angle on wave focusing, (*b*) the corresponding measured results from folding angle influence, (*c*) the influence of relative shortest distance from activated facets to the central axis on the analytical sound pressure levels, and (*d*) the corresponding measured results from the influence of activated facet distance to the central axis

that full area activation on a given facet cannot be realized experimentally. For axial distances greater than 0.2 m, the qualitative agreement is not as good between the analytical and experimental results. This is due to a combination of the effects from diffraction, reflection, and the directly radiated waves. It is expected that as the folding angle of the activated facets increases, the peak SPL and corresponding axial location increases and decreases, respectively. This is because increasing the facet folding angle reduces the convergent region for the radiated sound field and positions it closer to the plane of the unfolded array.

Figure 3(*c*) compares the analytical axial SPL for the Bricard-Miura and inverted Bricard-Miura array configurations for a 25-deg folding angle and 19-kHz driving frequency. The analytical results show that the Bricard-Miura array has a peak SPL around 67 dB at 0.1 m along the center axis, and the inverted Bricard-Miura array has a peak SPL around 62 dB at a 0.19 m axial distance. Corresponding experimental results for both array configurations are shown in Fig. 3(*d*), where the Bricard-Miura and inverted Bricard-Miura array configurations have SPL peaks reaching 67 dB and 58 dB at axial distances of 0.06 m and 0.21 m, respectively. Both the analytical and experimental results show that the Bricard-Miura array has a higher peak SPL and closer axial distance to the unfolded plane in comparison to the inverted configuration despite the discrepancies in exact SPL and axial distance values. These discrepancies occur for the same reasons that are explained in the results shown in Figs. 3(*a*) and 3(*b*). The acoustic focusing trend for the increase in peak SPL and decrease in the axial distance is similar to the previously discussed folding angle influence, whereas now the size and position of the convergent region for the radiated sound field are due to the distance between the activated facets and the central axis of the array. This means that the convergent region reduces and is positioned closer to the unfolded array plane when the distance between activated facets and the center axis is reduced, similar to increasing the folding angle.

4 Studies and Discussions

4.1 Wave Focusing for Active Facet Configurations. One of the objectives of this research is to identify activated facet configurations for the Bricard-Miura array that permit acoustic wave focusing along the central axis of the array. There are three configurations with activated facets that are analyzed. These configurations are the Bricard-Miura array with 12 activated facets (six quadrilateral and six triangular), the Bricard-Miura array with six activated quadrilateral facets, and the inverted Bricard-Miura array with six activated quadrilateral facets. These three activated facet configurations are shown in Fig. 1(*c*) and in the insets of Fig. 4. Analytical models are determined for each of the candidate configurations at driving frequencies of 10 kHz and 19 kHz and facet folding angles of 15 deg and 25 deg. These driving frequencies have been selected for this study to demonstrate the versatility of the Bricard-Miura array in wave focusing for multiple driving frequencies with the same geometric dimensions. Results from the analytical models are presented for a 15-deg folding angle and 10-kHz driving frequency in Fig. 4(*a*), a 25-deg folding angle and 10-kHz driving frequency in Fig. 4(*b*), a 15-deg folding angle and 19-kHz driving frequency in Fig. 4(*c*), and a 25-deg folding angle and 19-kHz driving frequency in Fig. 4(*d*). The horizontal axes represent the locations of the sound pressure levels along the center axis in terms of the number of wavelengths, starting at the unfolded array plane.

Figure 4 shows that the Bricard-Miura array with six activated quadrilateral facets has higher SPL peaks and smaller axial distances in comparison to the inverted Bricard-Miura array for the specified driving frequencies and folding angles. This behavior is expected based on the results discussed in Sec. 3. The results in Fig. 4 also show that activating the six triangular facets in the Bricard-Miura array marginally increases the SPL peaks and axial distances. Furthermore, the results in Fig. 4 show that the focal range, defined as the axial distance where the SPL is no more

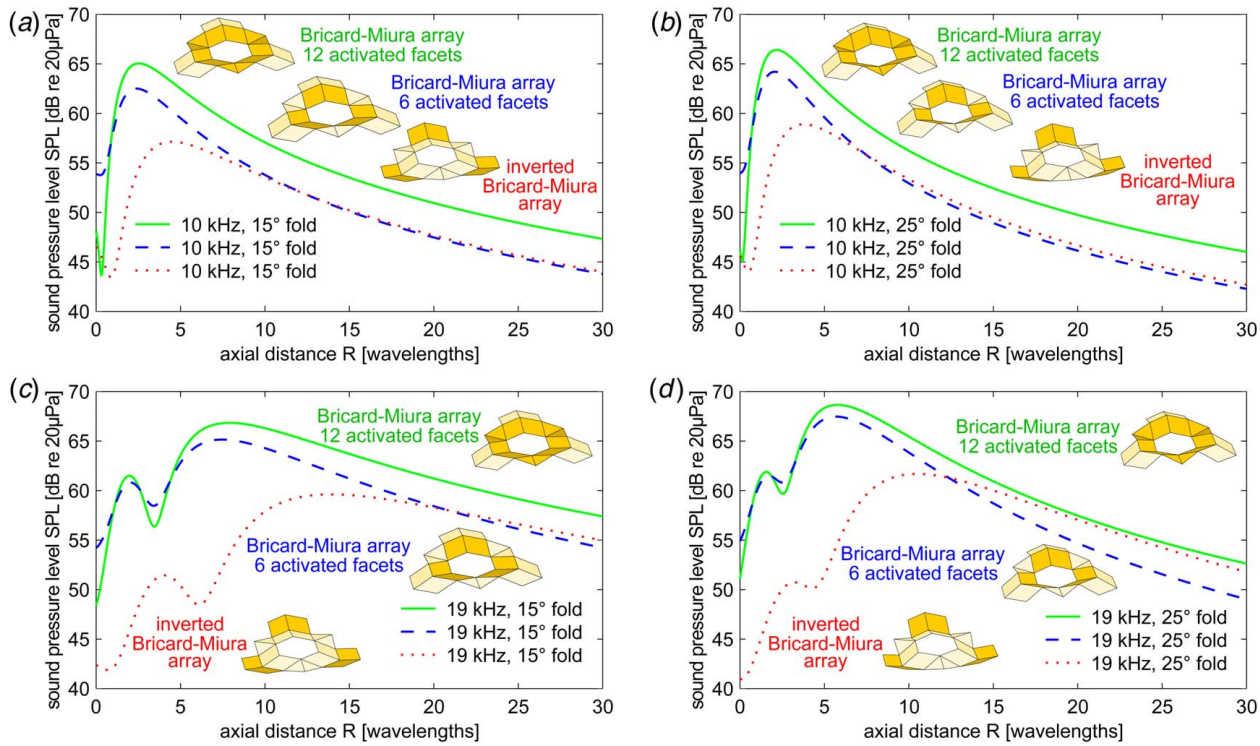

Fig. 4 Comparison of wave focusing from activated facet configurations for the Bricard-Miura and inverted Bricard-Miura array configurations for various driving frequencies and folding angles: (*a*) driven at a frequency of 10 kHz with a 15-deg folding angle, (*b*) driven at a frequency of 10 kHz with a 25-deg folding angle, (c) driven at a frequency of 19 kHz with a 15-deg folding angle, and (*d*) driven at a frequency of 19 kHz with a 25-deg folding angle

than 6 dB less than the peak SPL, varies for each array configuration, driving frequency, and folding angle.

A comparison of the results from Figs. 4(*b*) to 4(*a*) and 4(*c*) to 4(*d*) shows that the peak SPL increases and the axial distance decreases as the folding angle increases for the three array configurations, similar to the preliminary results in Fig. 3. The results from Figs. 4(*a*) and 4(*b*) show that the focal range decreases from 6.9 to 5.5 wavelengths for the 12 activated facet Bricard-Miura array configuration with an increase in folding angle from 15 deg to 25 deg. The focal ranges for the six activated facet Bricard-Miura and inverted Bricard-Miura array configurations also decrease from 6.5 to 5.1 wavelengths and 11.6 to 9 wavelengths, respectively. A decrease in focal range for the three activated facet configurations is expected due to the increasing folding angle that intuitively reduces the convergent region of the sound field. Comparing the results of Fig. 4(*c*) to those of Fig. 4(*d*) shows a decrease in the focal range from 16.1 to 9.7 wavelengths, 14.8 to 8.9 wavelengths, and 23.5 to 16.2 wavelengths, for the 12 activated facet, six activated facet, and inverted Bricard-Miura array configurations, respectively. A decrease in the focal range is also expected at this driving frequency for the same reasons that are previously explained.

A comparison of the results in Fig. 4 shows that increasing the driving frequency increases the peak SPL and corresponding axial distance, as well as the focal range. Increasing the folding angle also increases the peak SPL, yet decreases the axial distance and focal range of the peak. Furthermore, the Fig. 4 results show that the Bricard-Miura array configuration with 12 activated facets has the highest peak SPL in comparison to the other two configurations. This behavior is expected due to this configuration having a greater number of vibrating pistons contributing to the radiated sound field. Yet, the Bricard-Miura array configuration with six activated quadrilateral facets has a smaller focal range, and the resulting peak SPL can be increased to match that of the 12 activated facets configuration simply by increasing the normal surface velocity amplitude of the facets. Either of these activated facet configurations for the Bricard-Miura array is ideal for acoustic wave focusing, with the six activated quadrilateral facets configuration having a marginally smaller focal range.

4.2 Analysis of Convergence Regions for Active Facet Configurations. To further understand how the activated facets affect the acoustic wave focal range, the facet normal convergence area is analyzed for each configuration. The facet normal convergence area is the two-dimensional region where the normal vectors of the facets converge at the axial position of the peak SPL. Figure 5 shows the facet normal convergence areas for the

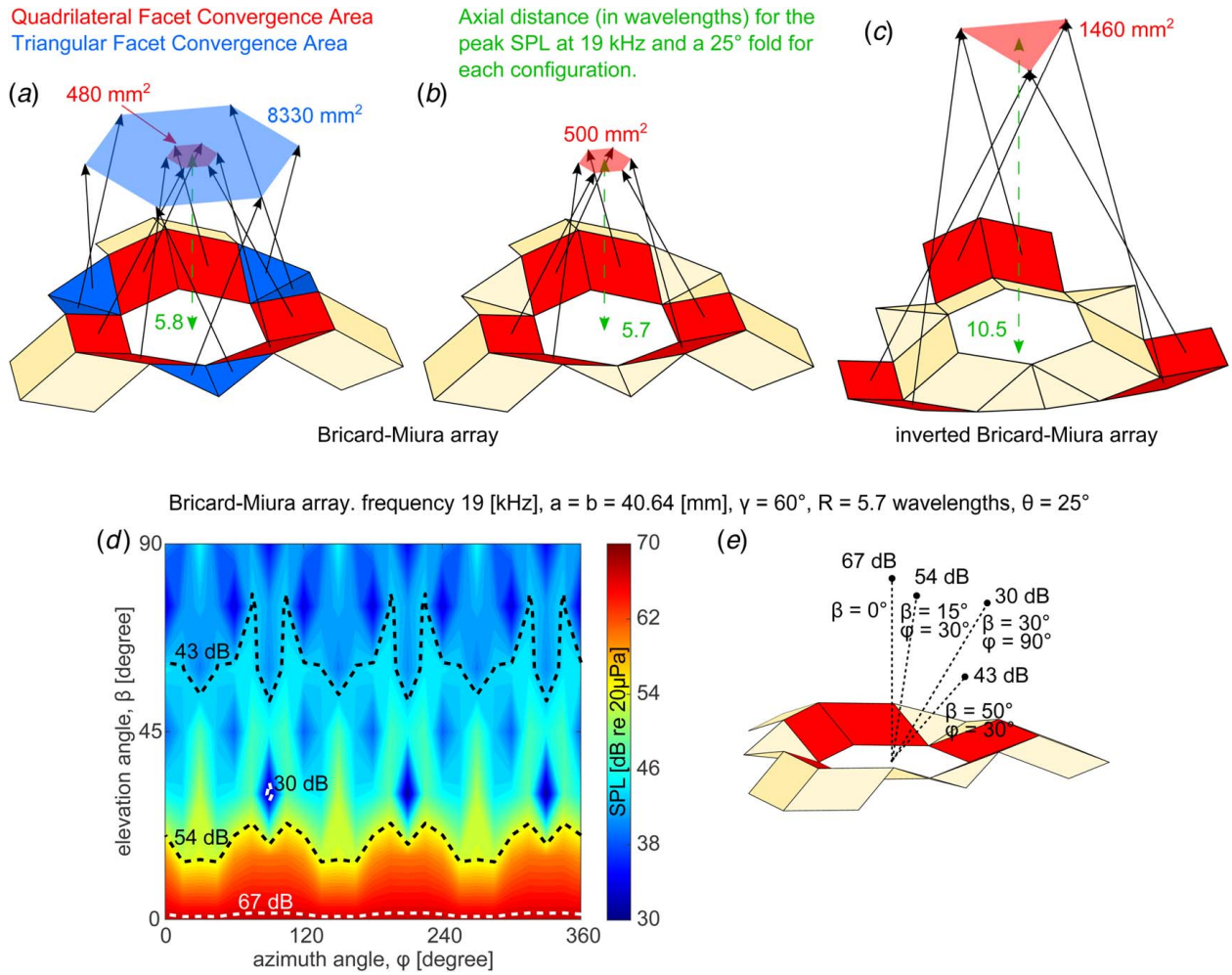

Fig. 5 Comparison of facet normal convergence regions analyzed at the axial position of the peak SPL for each activated facet configuration: (*a*) the convergence region for the Bricard-Miura array configuration with 12 activated facets, (*b*) the convergence region for the Bricard-Miura array configuration with six activated facets, (*c*) the convergence region for the inverted Bricard-Miura array configuration, (*d*) plot showing the influences of the elevation and azimuth angles on the SPL at a fixed radial distance of 5.7 wavelengths for the Bricard-Miura array with six activated quadrilateral facets, and (*e*) examples of the influence of the elevation and azimuth angles on the SPL overlaid on the Bricard-Miura array with six activated quadrilateral facets

three array configurations at a driving frequency of 19 kHz and a 25-deg folding angle, as well as the influences of the elevation angle, β, and the azimuth angle, φ, on SPL focusing for the Bricard-Miura array with six activated quadrilateral facets. The convergence area for each configuration is where normal vectors for the activated facets are extended to the axial position of the peak SPL. The end coordinates of the normal vectors form a six-sided area. This area is the convergence region. Figure 5(*a*) shows that the Bricard-Miura array configuration with 12 activated facets has two convergence areas of 480 mm^2 and 8330 mm^2. These areas suggest that the quadrilateral facets in red (dark shading) converge toward the center axis, and the triangular facets in blue (light shading) converge toward each other instead of the center axis of the array. Figure 5(*b*) shows that the Bricard-Miura array configuration with six activated quadrilateral facets has a convergence area of 500 mm^2. This is marginally greater than that of the quadrilateral convergence area in Fig. 5(*a*) and is due to the axial distance being smaller (5.7 versus 5.8 wavelengths), as it is seen in Figs. 5(*a*) and 5(*b*). Figure 5(*c*) shows that the inverted Bricard-Miura array configuration has a convergence area of 1460 mm^2.

Comparing the quadrilateral facet convergence areas for each configuration alongside the focal range results from Fig. 4(*d*) suggests that the Bricard-Miura array with either activated facet configuration has a smaller wave focal range and higher peak SPL than that of the inverted Bricard-Miura array configuration. This is because the Bricard-Miura array normal vectors converge closer to the central axis than for the inverted array counterpart. A comparison of Figs. 5(*a*) to 5(*b*) alongside the results from Fig. 4(*d*) suggests that the inclusion of the triangular facets increases the peak SPL. Yet, including the triangular facets also increases the focal range because of the increased convergence region. Based on these observations, acoustic arrays with smaller convergence regions have higher SPL peaks and smaller focal ranges in comparison to arrays with larger convergence regions.

Figure 5(*d*) shows the influences of β and φ on the focused SPL of the Bricard-Miura array with six activated quadrilateral facets. The plot is generated using the same parameters that have been used for Fig. 5(*b*), with the exception of R being set equal to 5.7 wavelengths. As it is seen in Fig. 5(*d*), as β increases from 0 deg to 50 deg, the focused SPL of the Bricard-Miura array decreases from 67 dB to 43 dB when φ is equal to 30 deg. Figure 5(*d*) also shows that the focused SPL of the Bricard-Miura array decreases to 30 dB when β is equal to 30 deg, and φ is equal to 90 deg, 210 deg, and 330 deg. Figure 5(*e*) shows a few examples of the focused SPL from Fig. 5(*d*) overlaying the Bricard-Miura array geometry as SPL field points. A comparison of the field points in Figs. 5(*d*) and 5(*e*) confirm that the peak SPL focusing occurs at the center axis of the Bricard-Miura array, as it is suggested in Figs. 5(*a*)–5(*c*).

4.3 Influences of Array Geometric Parameters on Wave Focusing for the Bricard-Miura Array With Six Activated Quadrilateral Facets. Geometric parameters for the rigid Miura-ori facet also influence the wave focusing behavior of the acoustic array. Figure 6 shows the peak SPL and focal range results for the Bricard-Miura array configuration with six quadrilateral activated facets as a function of the facet angle, edge length ratio, and folding angle of the Miura-ori unit cell. The edge length ratio ranges from 0.5 to 2, with edge $b = 40.64$ mm. The facet folding angle ranges from 5 deg to 30 deg, and a driving frequency of 19 kHz is used to vibrate the activated facets. The facet angle γ is also set to 45 deg in Figs. 6(*a*) and 6(*b*), and 60 deg in

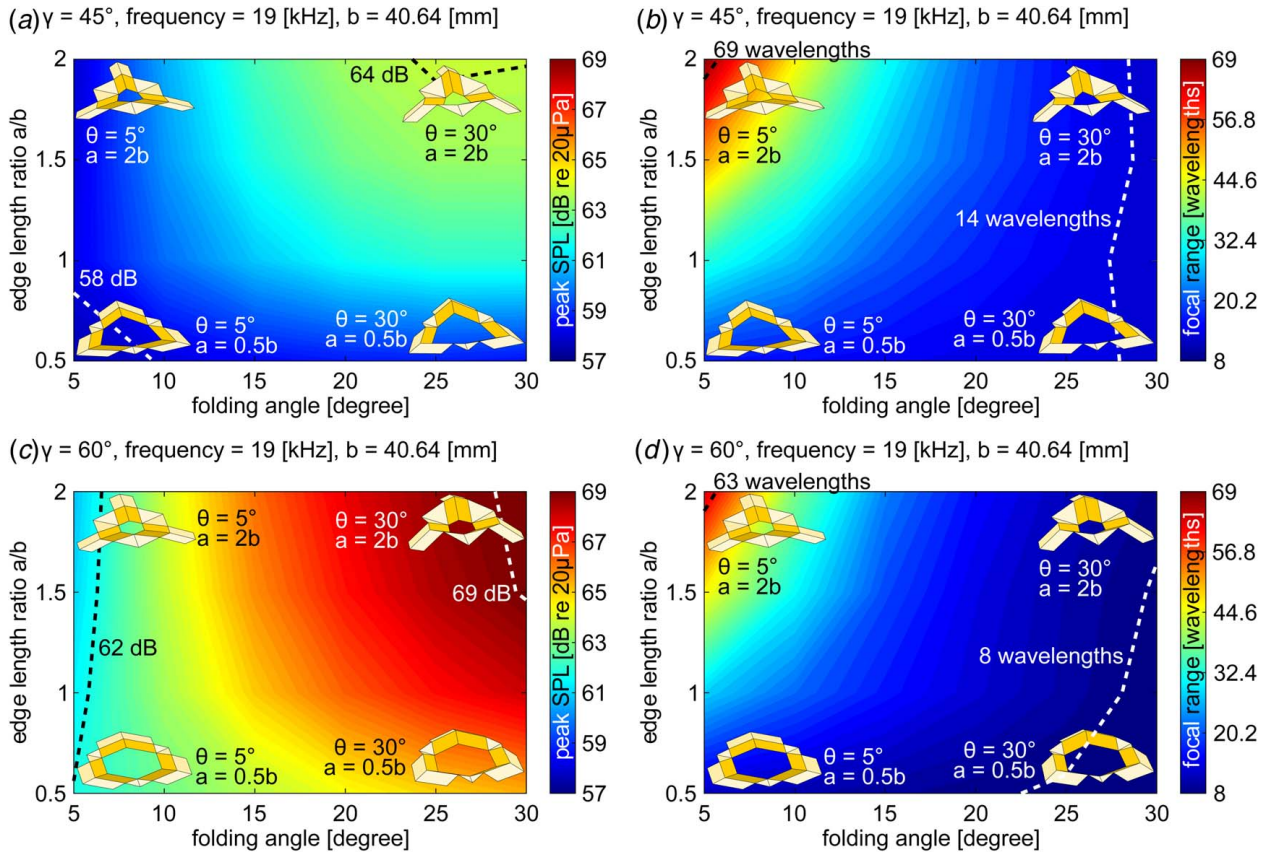

Fig. 6 Comparison of the influence of geometric parameters on peak SPL and focal range for the Bricard-Miura array: (*a*) the influence of varying edge lengths and folding angles on peak SPL for a 45-deg facet angle, (*b*) the influence of varying edge lengths and folding angles on focal range for a 45-deg facet angle, (c) the influence of varying edge lengths and folding angles on peak SPL for a 60-deg facet angle, and (*d*) the influence of varying edge lengths and folding angles on focal range for a 60-deg facet angle

Figs. 6(*c*) and 6(*d*). The insets in the corners of the subfigures for Fig. 6 represent the Bricard-Miura array when $a = 0.5b$ and $a = 2b$ for folding angles of 5 deg and 30 deg. Figure 6(*a*) shows that for a facet angle γ of 45 deg, the peak SPL increases from 58 to 64 dB as the folding angle and edge length ratio *a*/*b* increase. Note that when edge *a* is smaller than edge *b* the peak SPL only increases by no more than 1 dB as the folding angle increases. Figure 6(*b*) shows the corresponding focal ranges for the peak SPL values in Fig. 6(*a*), where the focal range is defined as being the axial distance range in which the SPL is no more than 6 dB less than the peak SPL. The results show that when $a \geq b$, increasing the folding angle decreases the focal range from 69 to 14 wavelengths. For a facet angle of 60 deg, Fig. 6(*c*) shows that the peak SPL increases from 62 dB to 69 dB as the folding angle increases from 5 deg to 30 deg, and the edge length ratio *a*/*b* increases from 0.5 to 2. Figure 6(*d*) shows the corresponding focal range results for Fig. 6(*c*). The results show that the focal range decreases from 63 to 8 wavelengths as the ratio *a*/*b* decreases from 2 to 0.5, and the folding angle increases from 5 deg to 30 deg.

A comparison of Figs. 6(*a*) to 6(*c*) demonstrates that increasing the facet angle from 45 deg to 60 deg increases the peak SPL of the Bricard-Miura array. This is due to larger activated areas contributing to the radiated sound field. Comparing Figs. 6(*b*) to 6(*d*) shows that increasing the facet angle from 45 deg to 60 deg also decreases the focal range, with the exception of increasing the focal range for folding angles around 5 deg. Furthermore, the focal range of the array reduces quicker as the folding angle increases, when comparing the results for the 60-deg facet angle to the results for the 45-deg facet angle. A decrease in the focal range from an increase in the facet angle occurs because the larger facet angle aligns the activated facet areas so that the emitted waves converge closer together. Alignment of the activated facet areas means that deviation in the shortest distance to the central axis for each facet is reduced. Improvement in the facet area alignment, for an increase in facet angle from 45 deg to 60 deg, can be seen by comparing the bottom insets in Figs. 6(*a*) and 6(*b*) to the corresponding insets Figs. 6(*c*) and 6(*d*). Similarly, when edge *a* is reduced to be smaller than edge *b*, the focal range of the peak SPL reduces because deviation in the shortest distance of the activated facets to the central axis is reduced. This can be seen by comparing the top insets to the bottom insets in Fig. 6(*d*).

5 Conclusion

This research explores a reconfigurable acoustic array inspired from a single-degree-of-freedom linkage and origami structure with shape changes that promote acoustic wave focusing. The analytical results show that acoustic arrays inspired from a Miura-ori and modified threefold-symmetric Bricard linkage synthesis are capable of wave focusing. Experiments are conducted with proof-of-concept models to validate analytical results for wave focusing. The peak SPL and focal range behaviors of the array are scrutinized for varying facet geometric parameters and principles of ray acoustics are leveraged for interpretation. The results show that the relative shortest distance of the facets to the center axis enhances the focal range when decreased. This research motivates the exploration of other reconfigurable acoustic arrays synthesized from origami structures and single-degree-of-freedom linkages for acoustic wave guiding functionality.

Acknowledgment

This project is supported by the National Science Foundation Faculty Early Career Development Award (Grant No. 2054970).

Conflict of Interest

There are no conflicts of interest.

Data Availability Statement

The authors attest that all data for this study are included in the paper.

References

[1] Chen, T., Bilal, O. R., Lang, R. J., Daraio, C., and Shea, K., 2019, "Autonomous Deployment of a Solar Panel Using Elastic Origami and Distributed Shape-Memory-Polymer Actuators," Phys. Rev. Appl., **11**(6), p. 064069.

[2] Pehrson, N. A., Ames, D. C., Smith, S. P., Magleby, S. P., and Arya, M., 2020, "Self-Deployable, Self-Stiffening, and Retractable Origami-Based Arrays for Spacecraft," AIAA J., **58**(7), pp. 3221–3228.

[3] Sim, Y. H., Yun, M. J., Lee, D. Y., and Cha, S. I., 2021, "Origami-Foldable Tessellated Crystalline-Si Solar Cell Module With Metal Textile-Based Stretchable Connections," Sol. Energy Mater. Sol. Cells, **231**, p. 111318.

[4] Kaddour, A., Velez, C. A., Hamza, M., Brown, N. C., Ynchausti, C., Magleby, S. P., Howell, L. L., and Georgakopoulos, S. V., 2020, "A Foldable and Reconfigurable Monolithic Reflectarray for Space Applications," IEEE Access, **8**, pp. 219355–219366.

[5] Hwang, M., Kim, G., Kim, S., and Jeong, N. S., 2021, "Origami-Inspired Radiation Pattern and Shape Reconfigurable Dipole Array Antenna at C-Band for CubeSat Applications," IEEE Trans. Antennas Propag., **69**(5), pp. 2697–2705.

[6] Espinal, F. A., Huff, G. H., Pallampati, S., Sessions, D., Fuchi, K., Bazzan, G., Seiler, S. R., Buskohl, P. R., Cook, A. B., and Gillman, A. S., 2020, "Circularly-Polarised Origami-Inspired Folding Patch Antenna Sub-Array," IET Microw. Antennas Propag., **14**(11), pp. 1262–1271.

[7] Banerjee, H., Li, T. K., Ponraj, G., Kirthika, S. K., Lim, C. M., and Ren, H., 2020, "Origami-Layer-Jamming Deployable Surgical Retractor With Variable Stiffness and Tactile Sensing," ASME J. Mech. Rob., **12**(3), p. 031010.

[8] Langford, T., Mohammed, A., Essa, K., Elshaer, A., and Hassanin, H., 2021, "4D Printing of Origami Structures for Minimally Invasive Surgeries Using Functional Scaffold," Appl. Sci., **11**(1), p. 332.

[9] Sargent, B., Butler, J., Seymour, K., Bailey, D., Jensen, B., Magleby, S., and Howell, L., 2020, "An Origami-Based Medical Support System to Mitigate Flexible Shaft Buckling," ASME J. Mech. Rob., **12**(4), p. 041005.

[10] Chauhan, M., Chandler, J. H., Jha, A., Subramaniam, V., Obstein, K. L., and Valdastri, P., 2021, "An Origami-Based Soft Robotic Actuator for Upper Gastrointestinal Endoscopic Applications," Front. Robot. AI, **8**, p. 119.

[11] Yi, J., Chen, X., Song, C., Zhou, J., Liu, Y., Liu, S., and Wang, Z., 2019, "Customizable Three-Dimensional-Printed Origami Soft Robotic Joint With Effective Behavior Shaping for Safe Interactions," IEEE Trans. Robot., **35**(1), pp. 114–123.

[12] Kim, Y., Lee, Y., and Cha, Y., 2021, "Origami Pump Actuator Based Pneumatic Quadruped Robot (OPARO)," IEEE Access, **9**, pp. 41010–41018.

[13] Melancon, D., Gorissen, B., Garcia-Mora, C. J., Hoberman, C., and Bertoldi, K., 2021, "Multistable Inflatable Origami Structures at the Metre Scale," Nature, **592**(7855), pp. 545–550.

[14] Balanis, C. A., 2016, *Antenna Theory: Analysis and Design*, Wiley, Hoboken, NJ.

[15] Williams, E. G., 1999, *Fourier Acoustics: Sound Radiation and Nearfield Acoustical Holography*, Academic Press, San Diego, CA.

[16] Kennedy, J. E., 2005, "High-Intensity Focused Ultrasound in the Treatment of Solid Tumors," Nat. Rev., **5**(4), pp. 321–327.

[17] Srinivas, V., and Harne, R. L., 2020, "Acoustic Wave Focusing by Doubly Curved Origami-Inspired Arrays," J. Intell. Mater. Syst. Struct., **31**(8), pp. 1041–1052.

[18] Zou, C., and Harne, R. L., 2020, "Deployable Tessellated Transducer Array for Ultrasound Focusing and Bio heat Generation in a Multilayer Environment," Ultrasonics, **104**, p. 106108.

[19] Zhao, N., Zou, C., and Harne, R. L., 2021, "Partially Activated Reconfigurable Arrays to Guide Acoustic Waves," J. Intell. Mater. Syst. Struct., **32**(20), pp. 2529–2540.

[20] Zhao, N., and Harne, R. L., 2021, "Reconfigurable Acoustic Arrays With Deployable Structure Based on a Hoberman-Miura System Synthesis," ASME J. Mech. Des., **143**(6), p. 063301.

[21] Lang, R. J., Brown, N., Ignaut, B., Magleby, S., and Howell, L., 2020, "Rigidly Foldable Thick Origami Using Designed-Offset Linkages," ASME J. Mech. Rob., **12**(2), p. 021106.

[22] Vlachaki, E., and Liapi, K. A., 2021, "Folded Surface Elements Coupled With Planar Scissor Linkages: A Novel Hybrid Type of Deployable Structures," Curved Layer. Struct., **8**(1), pp. 137–146.

[23] Chen, Y., Lv, W., Peng, R., and Wei, G., 2019, "Mobile Assemblies of Four-Spherical-4R-Integrated Linkages and the Associated Four-Crease-Integrated Rigid Origami Patterns," Mech. Mach. Theory, **142**, p. 103613.

[24] Feng, H., Peng, R., Zang, S., Ma, J., and Chen, Y., 2020, "Rigid Foldability and Mountain-Valley Crease Assignments of Square-Twist Origami Pattern," Mech. Mach. Theory, **152**, p. 103947.

[25] Chen, Y., Feng, H., Ma, J., Peng, R., and You, Z., 2016, "Symmetric Waterbomb Origami," Proc. R. Soc. A: Math. Phys. Eng. Sci., **472**(2190), p. 20150846.

[26] Zhang, X., and Chen, Y., 2018, "Mobile Assemblies of Bennett Linkages From Four-Crease Origami Patterns," Proc. R. Soc. A: Math. Phys. Eng. Sci., **474**(2210), p. 20170621.

[27] Gu, Y., Wei, G., and Chen, Y., 2021, "Thick-Panel Origami Cube," Mech. Mach. Theory, **164**, p. 104411.
[28] Wang, C., Li, J., and Zhang, D., 2021, "Optimization Design Method for Kirigami-Inspired Space Deployable Structures With Cylindrical Surfaces," Appl. Math. Model., **89**, pp. 1575–1598.
[29] Chen, Y., You, Z., and Tarnai, T., 2005, "Threefold-Symmetric Bricard Linkages for Deployable Structures," Int. J. Solids Struct., **42**(8), pp. 2287–2301.
[30] Yang, F., You, Z., and Chen, Y., 2020, "Foldable Hexagonal Structures Based on the Threefold-Symmetric Bricard Linkage," ASME J. Mech. Rob., **12**(1), p. 011012.
[31] Schenk, M., and Guest, S. D., 2013, "Geometry of Miura-Folded Metamaterials," Proc. Natl. Acad. Sci. U. S. A., **110**(9), pp. 3276–3281.
[32] Harne, R. L., and Lynd, D. T., 2016, "Origami Acoustics: Using Principles of Folding Structural Acoustics for Simple and Large Focusing of Sound Energy," Smart Mater. Struct., **25**(8), p. 085031.
[33] Zou, C., and Harne, R. L., 2019, "Tailoring Reflected and Diffracted Wave Fields From Tessellated Acoustic Arrays by Origami Folding," Wave Motion, **89**, pp. 193–206.
[34] Ocheltree, K. B., and Frizzell, L. A., 1989, "Sound Field Calculation for Rectangular Sources," IEEE Trans. Ultrason. Ferroelectr. Freq. Control, **36**(2), pp. 242–248.